Exp Fluids (2011) 51:731–741
DOI 10.1007/s00348-011-1091-5

RESEARCH ARTICLE

Experimental investigation into vortex structure and pressure drop across microcavities in 3D integrated electronics

Adrian Renfer · Manish K. Tiwari · Thomas Brunschwiler · Bruno Michel · Dimos Poulikakos

Received: 24 November 2010 / Revised: 12 February 2011 / Accepted: 28 March 2011 / Published online: 12 April 2011

Abstract Hydrodynamics in microcavities with cylindrical micropin fin arrays simulating a single layer of a water-cooled electronic chip stack is investigated experimentally. Both inline and staggered pin arrangements are investigated using pressure drop and microparticle image velocimetry (μPIV) measurements. The pressure drop across the cavity shows a flow transition at pin diameter–based Reynolds numbers (Re_d) ~200. Instantaneous μPIV, performed using a pH-controlled high seeding density of tracer microspheres, helps visualize vortex structure unreported till date in microscale geometries. The post-transition flow field shows vortex shedding and flow impingement onto the pins explaining the pressure drop increase. The flow fluctuations start at the chip outlet and shift upstream with increasing Re_d. No fluctuations are observed for a cavity with pin height-to-diameter ratio $h/d = 1$ up to $Re_d \sim 330$; however, its pressure drop was higher than for a cavity with $h/d = 2$ due to pronounced influence of cavity walls.

Electronic supplementary material The online version of this article (doi:10.1007/s00348-011-1091-5) contains supplementary material, which is available to authorized users.

A. Renfer · M. K. Tiwari · D. Poulikakos (✉)
Department of Mechanical and Process Engineering,
Laboratory of Thermodynamics in Emerging Technologies,
ETH Zurich, ML J 36, 8092 Zurich, Switzerland
e-mail: dimos.poulikakos@ethz.ch;
dimos.poulikakos@sl.ethz.ch

A. Renfer
e-mail: arenfer@ethz.ch

M. K. Tiwari
e-mail: mtiwari@ethz.ch

T. Brunschwiler · B. Michel
Advanced Thermal Packaging, IBM Research Laboratory,
8803 Rueschlikon, Switzerland
e-mail: tbr@zurich.ibm.com

B. Michel
e-mail: bmi@zurich.ibm.com

1 Introduction

High-performance next-generation multi-core processors require new architectures and advanced packaging. Vertical integration improves the bandwidth from core to cache memory, by reducing wiring length. Furthermore, it helps in obtaining a larger processor area, which effectively becomes the number of dies in the stack times the maximum projected lithography size for two-dimensional chips (Ulrich and Brown 2006). Therefore, the semiconductor industry is investing heavily into the development of through-silicon vias (TSV), which are the most important building blocks toward three-dimensional (3D) integration. However, in multi-layered, 3D packages, both heat flux and thermal resistances accumulate, resulting in junction temperatures above the reliability threshold. This constrains the electrical design and is the reason why thermal management is one of the key challenges for future microprocessor development. Interlayer water cooling is far superior to traditional air cooling techniques since it can remove the dissipated heat directly between the individual chip layers, promising performance increases for several device generations. The superior heat transfer capability of water notwithstanding the pumping power associated with the pressure drop across the chip is a criterion contributing to the overall energy costs for cooling 3D electronic chip stacks. To seal the electrical interconnects from water, the TSVs are embedded into silicon pins and the overall arrangement consists of a micropin fin array inside a microcavity. Therefore, the hydrodynamic investigation into

microfluidic chips with micropin fin arrays inside microchannels is of paramount importance in developing the next-generation integrated liquid cooling of 3D chip stacks.

Classically, for macroscale flows across a single cylinder, a critical Reynolds number marks the inception of vortex shedding. For an array of cylinders on the other hand, the flow field characteristics are more complicated, mainly due to interacting wakes (Ziada and Oengören 1993). In low aspect ratio (h/d) pin fin array cavities, the effect of confinement is expected to play an additional role, resulting in different flow regimes than in flows across cylinder arrays and cannot be described solely through a Reynolds number based on the cylinder diameter.

Flow across large-scale tube bundles with various configurations and shapes has been extensively investigated experimentally by several researchers using hot-wire or laser Doppler anemometry, PIV as well as pressure measurements. An overview of selected studies can be found in Paul et al. (2007). Iwaki et al. (2004) conducted PIV experiments using inline and staggered tube bundles ($d = 15$ mm) at Reynolds numbers of 5,400 and higher. They could identify three vortex structures behind the tubes; however, the vector fields were obtained by ensemble cross-correlation over 200 images. These studies focus on macroscale tubes, but the detailed hydrodynamics in micropin fin arrays confined in microchannels remains unexplored. Flows with low aspect ratio pin fins are likely to be different due to pronounced effects of cavity wall damping (Brunschwiler et al. 2009). Koşar et al. (2005) performed an experimental study on 100-μm-long micropin fin bundles with various configurations and reported on an increasing pressure slope at higher flow rate because of cylinder–wake interaction. These authors neither provided a detailed explanation for the pressure transition nor any flow visualization to support this observation. Prasher et al. (2007) observed a pressure gradient transition in the hydraulic performance of low aspect ratio micropin fins but did not provide a physical explanation. Brunschwiler et al. (2009) investigated various pin fin arrangements with different pin diameter, pitch and cavity heights for 3D integrated chip cooling. For inline and staggered distorted designs with a pitch and cavity height of 200 μm, they observed a clear flow regime transition through pressure measurements. No flow measurements were performed to investigate this transition. Alfieri et al. (2010) developed a hydrodynamics and conjugate heat transfer model of a single row of inline micropins in order to obtain correlations for modeling a 3D chip stacks simulator as a non-equilibrium porous media. No flow transition was considered. Liang et al. (2009) presented a numerical approach to simulate laminar flow across a row of six cylinders for different longitudinal pitches. They found a vortex shedding activity moving upstream with increasing pitch between the cylinders at a fixed Reynolds number. In the study of Nishimura et al. (1993), an upstream development of the transition to vortex shedding with increasing Reynolds number was observed in an array of inline and staggered large diameter tubes ($d = 15$ mm, $Re_d = 60$–$3{,}000$). No experimental visualization and measurement of the transition flow in micropin fin arrays confined in cavities has been reported to this date.

Herein, we report velocity and pressure drop measurements in micropin fin chips in inline and staggered distorted arrangement for flows with pin diameter–based Reynolds number (Re_d) up to 290. The velocity measurements are performed using microparticle image velocimetry (μPIV) for flow visualization at the microscale (Santiago et al. 1998; Wereley and Meinhart 2010). Instantaneous velocity field measurements required high microparticle seeding, which are prone to undesirable coagulation and sticking to solid boundaries of the flow domain (Lindken et al. 2009). In spite of these limitations, unsteady and/or turbulent flow dynamics in simple geometries such as micron size channels (Li and Olsen 2006a, b; Angele et al. 2006; Blonski et al. 2007; Natrajan and Christensen 2010), capillaries (Natrajan and Christensen 2007), obstacle-type valveless micropumps (Sheen et al. 2008), and inkjet print heads (Meinhart and Zhang 2000) have been previously reported by measuring instantaneous velocity fields. However, a complex geometry such as the microcavity with the micropin fin array considered here requires special care and techniques to avoid unwanted particle sticking. A novel pH-controlled, higher seeding of microparticles is employed to enhance signal-to-noise ratio in μPIV and to obtain instantaneous velocity measurements. The instantaneous μPIV measurements enabled us to perform unsteady flow characterization in such a complex microscale geometry as opposed to more common ensemble averaged μPIV measurements, which are only suited for steady state flows (Raffel et al. 2007). Detailed velocity data were obtained at different locations in micropin fin arrays, and vortex structures were analyzed in order to explain the pressure drop trend along the flow cavity. Furthermore, we show a position dependence of the pressure transition along the flow direction and the absence of vortex shedding for a cavity height equals pin diameter, in the Reynolds number domain investigated. The geometric sizes and flow rates selected to be studied are specifically suitable for integrated chip cooling. The corresponding pressure drop in such microcavities is essentially a necessary penalty of the chip cooling process. Our measurements show that the vortex shedding leads to a sharp rise in the pressure drop across the chip. However, vortices will also lead to enhanced mixing and heat transfer, thereby requiring a trade-off in the design of such chips. Through our work, we have identified these

competing aspects in designing microcavities with micropin fin arrays for integrated cooling of electronic chips.

2 Experimental setup

2.1 Microfluidic chip fabrication

The microfluidic chips were prepared using standard microfabrication techniques. Figure 1a, b shows pictures and schematics of the chips used in the study, respectively. The cylindrical micropin fins as well as the fluid ports were etched into silicon with deep reactive ion etching (DRIE) followed by anodic bonding of a 500-μm-thick glass plate to the top of the chip in order to form the cavity and still allowing optical access for μPIV. The resulting microfluidic chip cavity was square shaped in top-view (10×10 mm^2) with a height of 200 ± 10 μm. The pressure drop along the fluid path was probed using four pressure ports located at 0, 1, 5, and 10 mm along the flow direction (see Fig. 1a). The pressure ports at 0 and 10 mm are located within the cavity, 1 mm from the inlet/outlet as shown in the scanning electron microscope (SEM) image in the inset of Fig. 1a. The chip cavity was connected to a water loop using two rectangular 1-mm-wide inlet and outlet slots.

Two different cavity designs with 50×50 pins in the flow area of the chip were used as shown in Fig. 1b. The first is a pin fin inline (PFI) and the second a staggered distorted cell (PFS-dc) arrangement of pins; both with a pin pitch p of 200 ± 10 μm and a pin diameter d of 100 ± 5 μm ($p/d = 2$). Note that for the staggered distorted cell, every second column of pins is shifted by half a pitch in the flow direction.

2.2 Measurement method and experimental conditions

The flow was driven with an impeller pump (Conrad Electronic SE, Germany) to minimize pulsation, which could be the source of transient effects, at a maximum flow rate of 190 ml/min. The variation of the flow rate above 50 ml/min was less than 2%. The flow was measured with a laminar pressure gradient flow sensor (range: 0–500 ml/min; Omega, USA) with a full scale accuracy of 2%. A differential pressure gauge (range: 0–2.0 bar, accuracy: 0.2%; Omega, USA) was used to measure the pressure drop between the ports. All the pressure drop measurements were conducted at room temperature with de-ionized (DI) water as the working fluid. However, the pH of the water was adjusted using sodium hydroxide for μPIV experiments for the reasons described below. The pressure measurements were recorded with a delay of a few minutes after setting the flow rate, to ensure stabilization of flow through the flow loop. Figure 2 shows the flow loop and connected μPIV system used for flow visualization. The μPIV setup consisted of an epi-fluorescent microscope system (FlowMaster Mitas, LaVision, Goettingen, Germany) as shown in the figure. The test chips were placed on

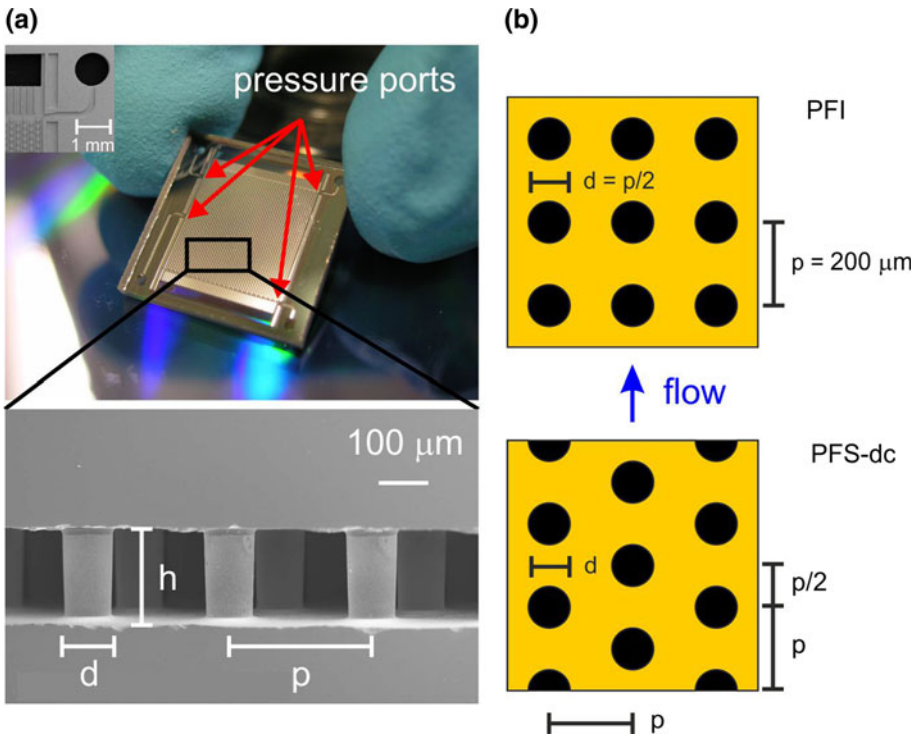

Fig. 1 **a** Photograph and SEM image of the microfluidic chip with the pressure ports indicted (*top*) and a SEM image of the micropin fins in the flow cavity (*bottom*). **b** Design of the inline (PFI) and staggered distorted cell (PFS-dc) chips used for the experimental study

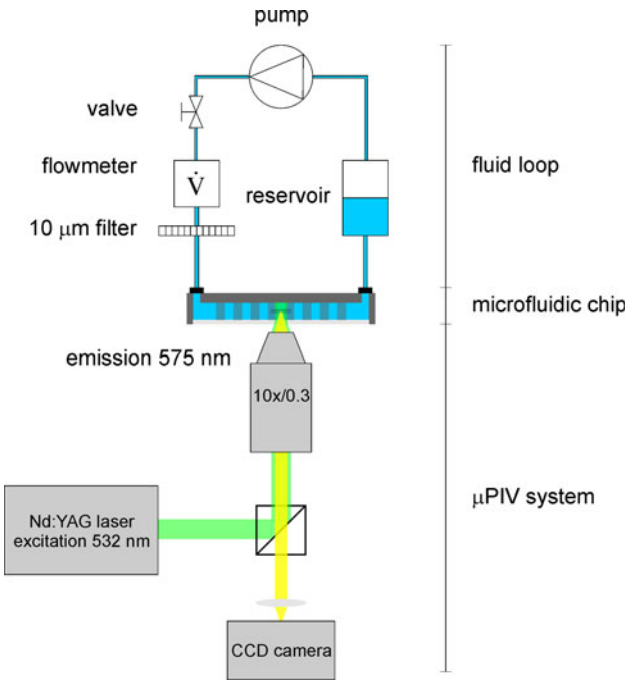

Fig. 2 Schematic of the μPIV system with the microfluidic chip connected to a water loop

the 3D stage of the epi-fluorescent microscope in order to change the location of the observed (focused) area. The flow was seeded with fluorescent buoyant particles (1 μm in diameter, Nile red FluoSpheres; Invitrogen, Carlsbad, CA). The tracer particles were excited with a double-pulsed 532 nm Nd:YAG laser, and the emitted light (575 nm) was recorded with a 2,048 × 2,048 pixel CCD camera. The energy per pulse was adjusted to approximately 10 mJ since the fluorescent signal saturated at higher pulse energies. Achieving instantaneous velocity fields from double-shot images requires a high seed particle density so that sufficient information is available for two-frame (double-shot) cross-correlation. In our measurements, in the absence of any further medication to DI water, particles stuck heavily onto the walls of the pins and the chip cavity.

This is a common challenge faced in μPIV experiments (Santiago et al. 1998) and result from Derjaguin and Landau, Verwey and Overbeek (DLVO)-type interaction, which accounts for both electric double-layer interaction and van der Waals attraction, between the particles flow boundaries (in our case pin surface and cavity walls) (Perry and Kandlikar 2008). The microspheres were charge stabilized by grafting proprietary polymers with pendant carboxylic acid groups. It is known that a convenient means to alter DLVO interaction is to alter the pH of the solution, which alters the double-layer interaction, thus stabilizing the charge-stabilized particles. We found that adjusting the water pH to ~9 using sodium hydroxide minimized the accumulation of anionic microspheres on micropins and cavity walls. The increased content of hydroxide ions (due to high pH) deprotonate the carboxylic groups on the microsphere surface such that the resulting negative charge on the particle prevents agglomerations. This step was crucial to obtaining instantaneous velocity measurements by cross-correlating the image pairs at any instant.

The timing of the laser illumination and frame acquisition were controlled using the LaVision software. The PIV image pairs (i.e., the double-shot images) were acquired with a frequency of 4 Hz. The time difference between the images of any pair was adjusted between 2 and 10 μs to yield a maximum particle displacement of approximately 1/4th of the initial interrogation window size of 256 × 256 pixels. This corresponds to a particle displacement of 18.8 μm. The intensity patterns from the fluorescent particles associated with the laser pulse was recorded on individual frames. To compute the velocity vectors, an adaptive multi-pass cross-correlation technique was used. Starting from an interrogation window of 256 × 256 pixels, the vector fields computed at every iterative pass were used to as to adjust the window shift for the following passes. The final interrogation windows of size 64 × 64 (18.8 × 18.8 μm) or 32 × 32 pixels (9.4 × 9.4 μm) with a 50% overlap, in both cases, were used. The resulting vector spacing was 9.4 μm (for 64 pixel windows) or 4.7 μm (for 32 pixel windows).The size of interrogation window is specified in the caption of all figures in Results and discussion section showing velocimetry measurements. For steady flows, ensemble averaged cross-correlation was performed with 68–100 image pairs depending on the flow situation and compared with instantaneous velocity fields from double-shot images. To reduce image random noise, the particle images were pre-processed with a 3 × 3 low-pass filter, and a spatial sliding minimum subtraction was used to remove background noise.

In this study, a 10× microscope objective with a numerical aperture of 0.3 was used for imaging providing a depth of correlation $2z_{\text{corr}} = 27.6$ μm (Olsen and Adrian 2000). The number of particles within an interrogation window of 64 × 64 pixels was chosen to be $n = 10$. Therefore, the volumetric particle concentration of the seeding particle was computed as

$$c_{\text{vol}} = 100 c V_{\text{particle}}, \tag{1}$$

where V_{particle} denotes the particle volume and c the number of particles in an interrogation depth, which was computed as $c = n/(2z_{\text{corr}}A_{\text{int}})$ with A_{int} designating the interrogation area. Substituting the numerical values, we obtain $c_{\text{vol}} = 0.054\%$.

Although the particle seeding was chosen to achieve a final interrogation window size of 64 × 64 pixels, some flow conditions allowed an additional refinement with a

final interrogation windows size of 32 × 32 pixels. This clearly resulted in better resolution in computed vector fields. However, since our particle seeding density was chosen for a final interrogation window size of 64 × 64 pixels, results from interrogation windows of 32 × 32 pixels were only taken into account if average velocity from these two different window size was within 1%. The specific interrogation window size is mentioned in every figure below to avoid any confusion.

3 Results and discussion

The hydrodynamics of the flow through the chips was investigated through pressure drop and velocimetry measurements as described next.

3.1 Pressure drop measurements

The pressure drop measurements across the entire chip for two different micropin fin arrangements are shown in Fig. 3 as a function of the Reynolds number, Re_d defined in terms of pin diameter d as

$$\mathrm{Re}_d = {}^{v_\mathrm{m} d}/_{\nu}, \tag{2}$$

where ν is the kinematic viscosity of water and v_m the mean velocity of the fluid between the pins. For any flow rate $\dot{V}$, the mean velocity can be computed as

$$v_\mathrm{m} = \dot{V}/\big(h(p-d)N_\mathrm{p}\big) \tag{3}$$

where the symbols h, p, and N_p denote the cavity height, pin pitch, and number of pins, in a cross-section normal to the flow direction, respectively. The pressure drop variation as a function of Reynolds number shows a sharp change in the slope for both pin fin configurations at $Re_d \approx 200$ (135 ml/min).

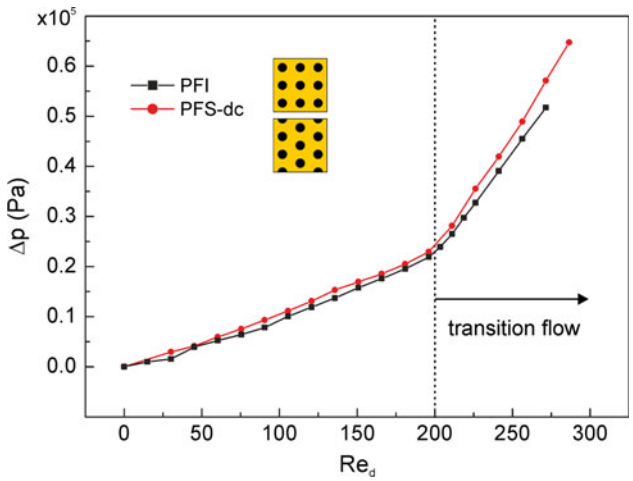

Fig. 3 Relative pressure drop across the entire chip for the inline and staggered-dc configuration. At $Re_d \approx 200$, a pressure gradient change indicates a flow regime transition

As will become clear after the μPIV results described later, this transition is clearly influenced by vortex dynamics in fluid flow beyond these critical Re_d. The strong slope increase after $Re = 200$ (Fig. 3) is problematic for microfluidic electronic cooling applications since it may result in an excessive overall pressure drop. However, as a beneficial effect, such flow regime was found to be responsible for improved heat transfer as reported by (Brunschwiler et al. 2009). Micropin fin–based chips simulate the integrated cooling strategy which is the only feasible means to address the cooling needs of the next-generation 3D chips. Therefore, it is critical to understand the nature of this transition.

As a first step toward understanding the transition in Fig. 3, the variation in differential pressure drop across the length of the chip was investigated. Figure 4 presents the results of these local (at certain predefined portions of the chip) pressure drop measurements only for the chip with the inline fin arrangement (PFI), since the global pressure curve was similar for the staggered arrangement (PFS-dc). The pressure drops near the inlet and outlet are measured across five transversal pin rows, whereas nearly 20 transversal pin rows each are covered for two measurements in the middle. These measurements are designated in Fig. 4a as inlet, outlet, middle 1, and middle 2. Due to the symmetry of the measurement ports, the local pressure measurements were repeated by reversing the flow direction (changing inlet to outlet and vice versa). With these measurements, it was possible to reveal the position dependence of the transition across the chip.

The onset of the transition in terms of Re_d propagates spatially in response to higher Reynolds numbers (corresponding to higher flow rates) from the outlet to the inlet. In other words, the location of flow transition moved upstream with rise in flow rates; the onset of the transition $Re_d \approx 180$, 200, and 250 for outlet, middle 2, and middle 1 locations, respectively. At the inlet, the transition did not happen even at the highest flow rate investigated (180 ml/min, i.e. $Re_d \approx 270$).

The pressure drop measurement conducted at the outlet over five transversal pin rows revealed more details about the gradual upstream movement of the flow transition, which is marked by vortex shedding (see the following section). It is clear from the inset in Fig. 4a that the transition is marked by two different slopes in pressure drop curve. From $Re_d = 180$ to 195, we observed a steeper rise in pressure drop than from $Re_d = 195$ upwards. This indicates that the onset of transition flow across these five transverse pin rows is gradual since vortex shedding starts from the downstream pins, with gradually more pins shedding vortices with increasing flow rate (Re_d). The vortex shedding process will become clearer after the

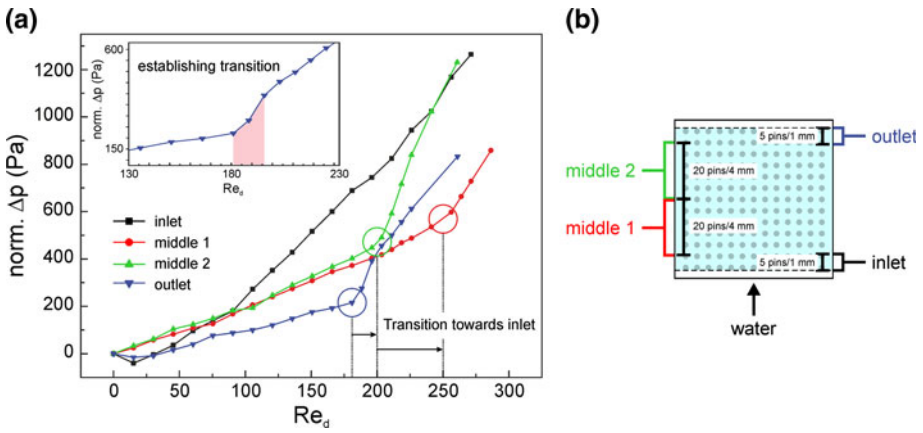

Fig. 4 **a** Variation in pressure drop per transversal unit row with Re_d for the inline configuration. The normalized value of the pressure drop was extracted from the differential pressure drops measured across different sections shown in part **b**). An increased slope in the pressure drop marks the transition. The details of the transition zone are shown in the *inset*. The onset of the transition moves upstream for higher Reynolds numbers (marked by *arrows*) but was not observed at the *inlet* even at $Re_d = 270$. **b** Schematic of the differential pressure measurement sections on the chip

discussion on the results of the instantaneous μPIV measurements described below. Once complete transitional flow (with vortex shedding from all five pin rows) is established, only the increased mass flow contributes to the rise in pressure drop. Note that the onset of the transition at the outlet ($Re_d \approx 180$) is hardly visible in the overall pressure drop measurement across the entire chip (c.f. Fig. 3). This is simply due to a lower amount pressure drop across the five transverse pin rows compared with the overall chip consisting of 50 rows. The two different slopes do not appear in the post-transition measurements in Fig. 3 because for the range of flow rate considered here no transition occurred at the inlet of the chips.

As a consistency check, the local pressure drop measurements were summed up and compared to global measurements across the entire chip. The resulting error was around 1%.

3.2 μPIV measurements

3.2.1 Steady flow

In order to understand the sharp transition in pressure drop with flow rate, the μPIV measurements were performed on the pin fin arrays before and after the transition. Since the pressure drop transition was position dependent, the velocimetry was performed close to the inlet and outlet and at the center of the chip cavity in the streamwise direction at $h/2$. Before the transition, the flow through the chips was found to be steady and stagnant symmetric vortices formed behind the

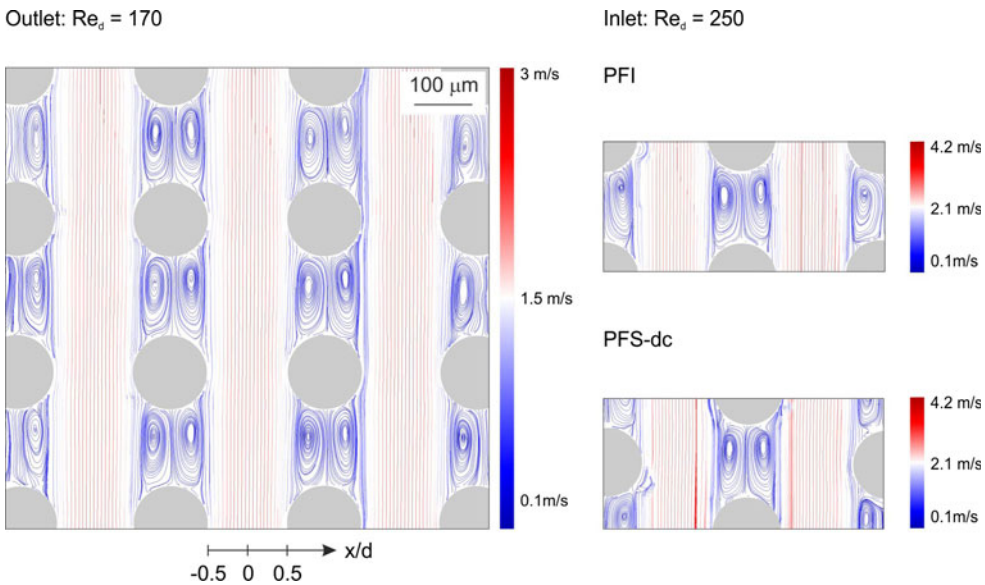

Fig. 5 Ensemble-averaged streamline pattern of the steady flow across the inline pin fin array (final interrogation window 32 × 32 pixels). For flow rates below the critical Reynolds number, a stable pair of vortices is formed in the space between the pins in the flow direction for both inline and staggered-dc pin arrangement. Whereas the flow at the *outlet* starts fluctuating at $Re_d = 180$, the recirculation zones at the *inlet* remain stable even at $Re_d = 250$

pins in both inline and staggered-dc arrangements as shown in Fig. 5. The figure shows the streamline plots for measurements near outlet at $Re_d \approx 170$ and near inlet at $Re_d \approx 250$. Ensemble cross-correlation was used to calculate the velocity vectors corresponding to Fig. 5; however, since the technique only works for steady flows, the correlation was also tested with double-shot cross-correlation as discussed below. The figure clearly shows that pre-transitional vector fields were characterized by two flow regions: a high velocity microchannel-like flow between the pins in the longitudinal streamwise direction and a recirculation zone behind the pins. The steady nature of the flow before the transition can be further appreciated by looking at the streamwise velocity profiles, for different locations along the flow direction, plotted in Fig. 6a. The origin of the normalized x-coordinate plotted in Fig. 6 is shown in Fig. 5. The profiles show the streamwise velocity of the channel-like flow at $Re_d = 143$ averaged over a distance of four pins in flow direction at different positions on the chip. The velocity profiles evaluated by ensemble averaged cross-correlation and double-shot cross-correlation are compared in Fig. 6b. The ensemble averaged velocity profile was computed by taking an ensemble average over 68 image pairs. The individual double-shot cross-correlations are averaged to obtain a mean profile, plotted as black symbols in Fig. 6b, which coincides with the ensemble averaged profile. The black error bars indicate the maximum deviations of individual cross-correlated velocities at any location from the mean. The deviation of the double-shot cross-correlations from ensemble averaged profile (indicated by error bars in Fig. 6b) is lower than 4.5%. It is important to keep in mind that the error bars also include the influence of the small inaccuracy of the water pump to maintain a constant flow rate. Therefore, the velocimetry analysis itself is expected to be more accurate than the error bars in Fig. 6b indicate.

3.2.2 *Transition flow*

After the transition, the flow pattern becomes very complex and the velocity field is strongly disturbed by transversal fluctuations as shown in Fig. 7 (for more details, see supplementary movie). The time separation between individual image pairs was 5 μs. This means that we obtain a good picture of the instantaneous flow field; however, the information about the temporal evolution of the flow field is limited by a low acquisition frequency of image pairs (4 Hz in our experiments). This is a common problem of state-of-the-art μPIV measurements due to low signal-to-noise ratios in the individual PIV images. Given this limitation, the characteristic time scale of the fluctuations could not be measured. With instantaneous velocimetry, it was possible to obtain sample frozen patterns of the flow. Figure 7a shows instantaneous streamline patterns at $Re_d \approx 250$ at the center of the chip. The stagnant recirculation zones observed before the transition become unstable, and different vortex structures are observed behind the pins. Figure 7b shows some sample flow patterns observed such as a symmetrical pair of vortices and a single and a collapsed vortex between pins. These sample images indicate complex vortex structures and explain the higher post-transitional pressure drop. Whereas in steady flows stagnant symmetric vortices are the only structures observable, in the transition flow, the symmetric vortices are an intermediate state. The sample instantaneous images shown in Fig. 7b suggest that with time the bimodal flow structure, consisting of symmetric vortices and a microchannel-like flow in between the pins, gives way to a single vortex followed by a complete collapse of recirculation. This transition flow pattern was not observed at the inlet up to $Re_d = 250$. A simple means to recognize this fluctuating flow pattern is to plot the variation in velocity vector angle from the streamwise direction at the point of strong shedding. In Fig. 8, these angles are plotted for velocity vectors along the line of symmetry between pins in the streamwise direction at inlet, center, and the chip outlet for $Re_d = 250$. At the inlet, Fig. 8a, the deviation from the streamwise axis remains at $\pm 0.3°$. In the center of the chip, the transient vortex structure strongly enhances the oscillation of the velocity vector as shown in Fig. 8b. The deviation of the flow path is highest between the pins, and therefore, the maximum deviation of the vector angles is located at $y/d \approx 1$, 3, 5 (see Fig. 8b). Due to the constraints imposed by the inline

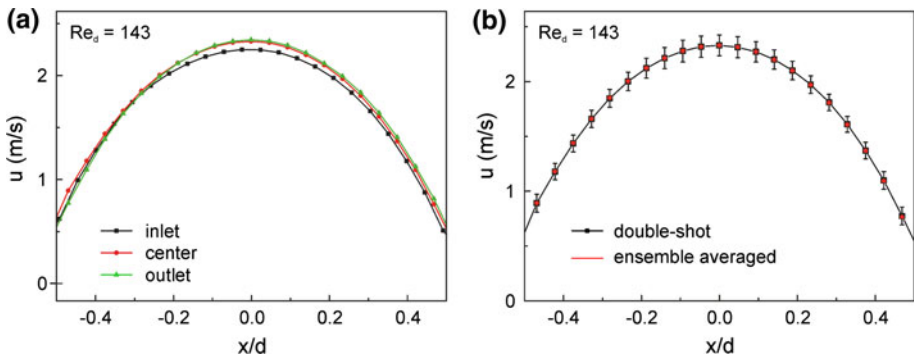

Fig. 6 **a** Pre-transitional streamwise ensemble averaged velocity profiles of the microchannel-like flow between the pins at the *inlet*, *center*, and the *outlet* (final interrogation window 32 × 32 pixels). **b** Averaged velocity profiles between pins from ensemble cross-correlated and double-shot frames. The RMS value of the instantaneous velocity profile is around 4.5%

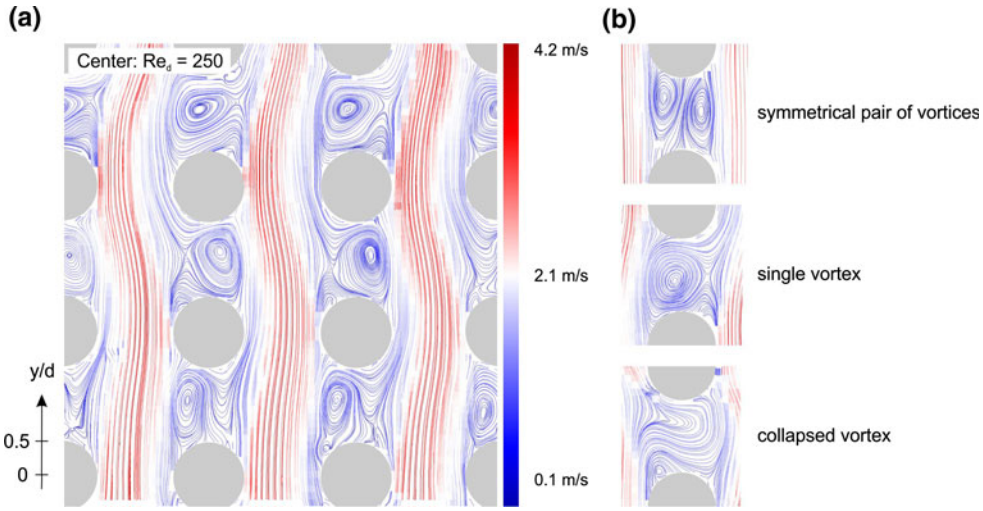

Fig. 7 **a** Streamlines showing the instantaneous vortex structure developed at the *center* of the PFI chip at $Re_d = 250$. **b** Selected samples of the different observed vortex structures between the pins. A final interrogation window of 64 × 64 pixels was chosen

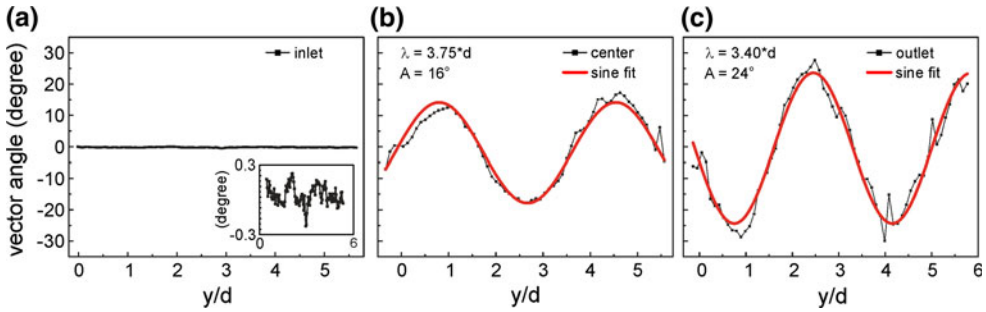

Fig. 8 Velocity vector angle fluctuation from the flow direction at midway between two longitudinal pin rows at $Re_d = 250$ using a final interrogation window of 64 × 64 pixels. **a** Vortex shedding at the *inlet* of the chip is completely absent (fluctuations less than 0.3°, see *inset*). Whereas in the *center* (**b**), the angle of the absolute velocity varies up to 16° (amplitude A of the *sine fit*), and at the *outlet*, the vortex shedding is amplified up to 24°. Note that all these profiles were drawn at the instant of maximum deviations of streamlines between the pin rows in the flow direction

geometry, the vector angle is nearly zero at the pin locations (pin center at $y/d = 0, 2, 4, 6$) and the wavelength of the vector deviation angle is almost exactly equal to twice the pitch, i.e. $\lambda \approx 2p$. The amplitude A of the deviation is 16° as shown in Fig. 8b. At the outlet, high deviations ($A = 24°$) in vector angle were observed, and due to the strong vortex shedding activity, λ becomes smaller than $2p$, as shown in Fig. 8c.

Due to the vortex structure described above, the streamwise velocity profile between pins also becomes significantly altered compared to the profiles for steady flow and becomes time dependent. Figure 9a shows sample instantaneous streamwise velocity profiles at different instants of the flow oscillation mode between two pins in the center of the chip. The corresponding streamlines along with marking for the location of velocity profile are shown in Fig. 9b. Clearly, the location of velocity maxima moves closer to the pins as the central fluid stream fluctuates around its mean position. Profile (i) and (iii) are the two extremes observed in our measurements.

Note that the mass flow rates computed using the instantaneous velocity profiles (after commencement of shedding) deviate up to 15% from the intermediate microchannel-like mass flow rate (area under the curve). This can be explained by variations of the shedding activity, which is strong enough to locally redirect the flow to the next parallel longitudinal pin row (c.f. Fig. 10). Additionally, a possible mass flow rate contribution due to three-dimensional rotation about the main axial flow direction is not captured in the measurements. However, the averaged velocity fields (computed from 100 instantaneous velocity fields across four pins) mass flow rate only deviated by 2% from the instantaneous microchannel-like mass flow.

3.2.3 *Flow impingement*

The transient vortex structure and the associated higher fluctuation in flow result in increased viscous dissipation. A second reason for enhanced post-transition pressure drop is flow impingement on to the pin walls as shown in Fig. 10. The increased flow oscillations in the center and the outlet of the chip redirect the flow path periodically. Such flow oscillations start gradually and increase with increasing Re_d;

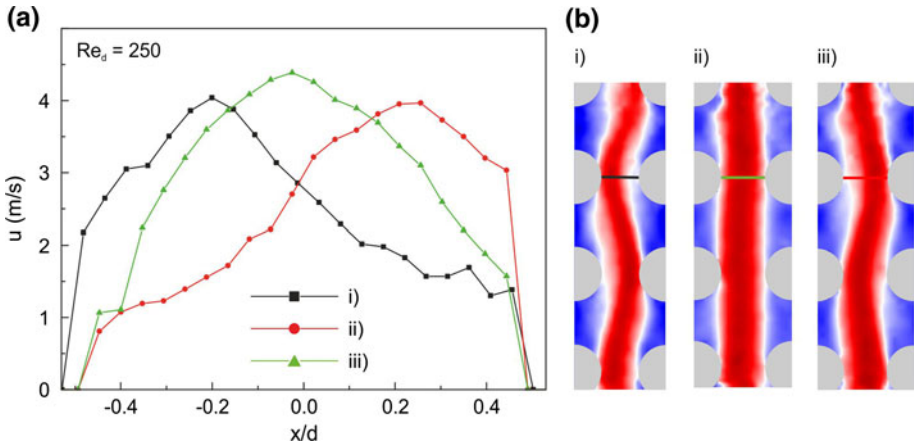

Fig. 9 **a** Instantaneous streamwise velocity profiles at different times of the vortex shedding cycle with the corresponding velocity pattern (the final interrogation window was 32 × 32 pixels). **b** The oscillation induces an inflection point in the profile since the maximum velocity is shifted closer to the pin in (*i*) and (*iii*) compared to the intermediate microchannel-like flow in (*ii*)

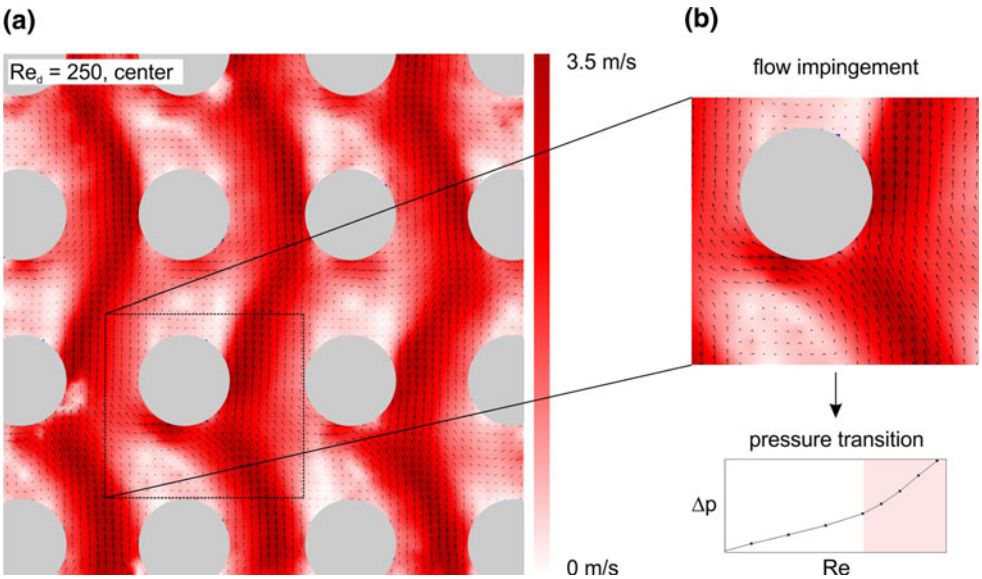

Fig. 10 **a** Flow impingement on pins contributing to the pressure drop transition, **b** zoomed in view of flow impingement on the pins. For vector calculation, the final interrogation window was 64 × 64 pixels

oscillations of a few degrees in the velocity vector are observed before the critical Re_d, (data not shown for brevity). Beyond the critical Re_d, however, the flow oscillations become strong enough to initiate flow impingement on the pins. The microchannel-like steady flow in between the pins before the transition appears to start oscillating post-transition and impinges alternatively on to the pins located on either side of it. This flow behavior is also marked by a complete collapse of the symmetric vortex structures between successive pins. The alternative flow impingement with the corresponding momentum change partly explains the increase in the pressure drop post-transition.

3.2.4 Confinement effects

For integrated electronic cooling, a small cavity is desirable to facilitate higher packaging density and shorter TSV length. On the other hand, for low aspect ratio microfluidic cavities chips with $h/d \leq 2$, the wall confinement may significantly affect the flow behavior as also noted in Koşar et al. (2005). We have also reported previously through the pressure drop measurements in Brunschwiler et al. (2009) that a clear transition is absent for the inline and staggered-dc micropin arrays with a height of 100 μm. Recently, Patil and Tiwari (2010) numerically investigated the flow past a square cylinder for different aspect ratios $0.5 \leq h/d \leq 3$. The confinement effect delayed the onset of vortex shedding and was only observed for $h/d \geq 2$ at Re = 600. Therefore, the decreased aspect ratio has a stabilizing effect on the wake behind the pins. As the boundary layer thickness is inversely related to the aspect ratio (Özdemir et al. 2009), for low *h/d* the boundary layer size can be of the order of the cavity height. In this regime complex, three-dimensional flow structures arise (e.g., horseshoe vortices) and may influence the alternating vortex shedding (Armellini et al. 2009).

To clarify whether the inception of vortex shedding is delayed due to the reduction in the aspect ratio for flows across micropin fin arrays, velocimetry measurements were compared between cavities with the staggered-dc pin array

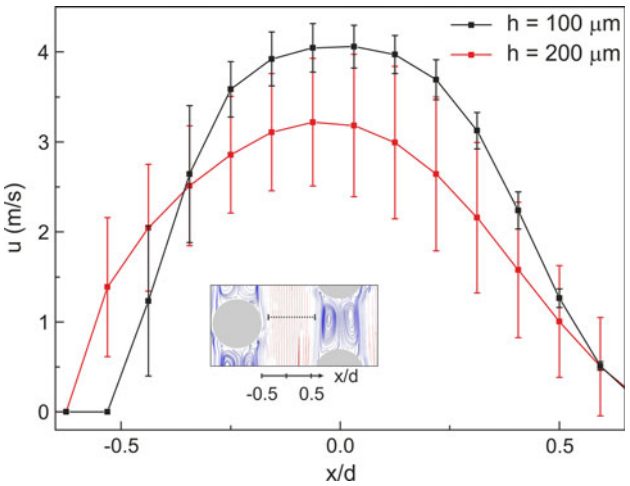

Fig. 11 Averaged streamwise velocity profiles for a staggered-dc micropin fin array with two different cavity heights. For $h/d = 2$, vortex shedding was observed while the small error bars for $h/d = 1$ show the absence of vortex shedding at $Re_d = 330$ ($Re_{dh} = 395$). For both cases, the final interrogation window was 64 × 64 pixels

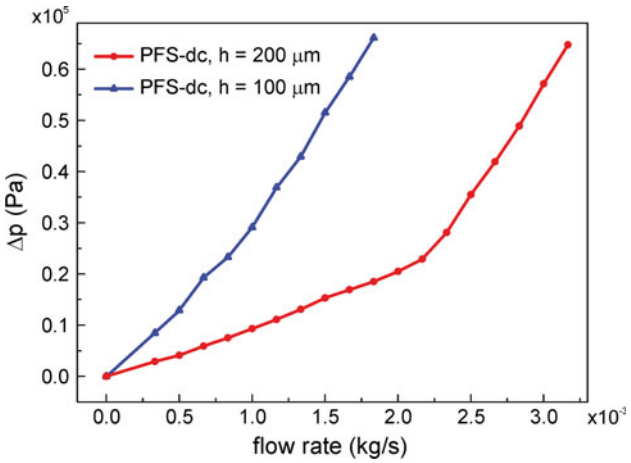

Fig. 12 Pressure drop curves for two different cavity heights 200 and 100 μm, respectively. Even though, no vortex shedding is observed for $h = 100$ μm, for the applied flow rates, the pressure drop and the associated pumping power are higher compared to a 200-μm cavity

with a height of 100 and 200 μm. The presence or absence of vortex shedding can be determined from the RMS value of the velocity fluctuations. For both cavities, the streamwise velocity profiles were averaged over 80 instantaneous velocity profiles between the pins (Fig. 11, dotted line in inset). For $h = 200$ μm, the vortex shedding caused the streamwise velocity component to fluctuate up to 25% at $x/d = 0$. For $h = 100$ μm, i.e., an aspect ratio $h/d = 1$, the corresponding deviation from the mean velocity is around ≈5%, which is comparable to the measurement accuracy (4.5%). Due to the pronounced shedding, the averaged streamwise velocity component for the cavity with $h = 200$ μm is lower. The inception of shedding across the entire staggered-dc chip with $h = 200$ μm starts at $Re_d \approx 200$ or based on the hydraulic diameter $d_h = 128$ μm (more details in Brunschwiler et al. (2009)) at $Re_{dh} \approx 275$. However, for $h = 100$ μm, no transitional flow was observed even up to $Re_d \approx 330$ (corresponding $Re_{dh} \approx 395$), demonstrating the inability of pin diameter–based Reynolds numbers as predictor of vortex shedding and a stronger role played by viscosity due to the confining influence of the cavity walls on the flow dynamics.

It is worth noting that for a cavity height $h = 200$ μm, the contribution of the additional wall friction arising from vortex shedding is still smaller compared to the viscous losses due to increased confinement for a cavity height $h = 100$ μm. The pressure drop curves for both cavity heights do not intercept for the investigated flow rates. Moreover, the slope for the 200-μm cavity in the transitional regime is similar to the pressure drop slope for $h = 100$ μm (Fig. 12). Therefore, the pressure drop associated with the pumping power to cool 3D electronic chip stacks is smaller for a 200-μm cavity for a wide range of flow rates, even though vortex shedding is present. Obviously, the penalty of using a higher cavity height is sacrificed on the level of miniaturization achieved in the vertical direction as well as an enhanced fabrication time and cost.

4 Conclusion

In conclusion, we investigated the hydrodynamics of flow across an assembly of micropin fins confined in a chip microcavity by means of pressure drop and μPIV measurements. The geometry simulates a typical single cavity out of vertically stacked, TSV-connected layers of 3D chips with integrated cooling structure to address the needs for next-generation integration challenge. Two different pin arrangements, inline and staggered distorted cell and two different cavity height-to-pin diameter ratios, 1:1 and 2:1, were evaluated. The pressure drop across the chip with a height-to-diameter ratio of 2:1 showed a flow regime transition, characterized by a considerably higher slope of pressure drop with respect to flow rate, at Reynolds number ≈200 based on the pin diameter. The flow field was analyzed both before and after the transition. A pH-controlled high seeding of PIV particles was used to obtain the instantaneous velocity field by cross-correlating PIV image pairs and to avoid using ensemble cross-correlation, which is only suitable for steady flows. Before the transition, the flow field was stationary with a characteristic channel-like flow between the pin rows in the flow direction and a stable vortex pair in between pins. For this steady flow, the double-shot (image pair) and ensemble averaged cross-correlations produced acceptably accurate velocity profiles (error <4.5%). After the transition, the flow was

characterized by a fluctuation of the flow field with strong flow impingement onto the pin walls explaining the sharp transition in the pressure drop. The flow fluctuations were location dependent and occurred first (for smaller flow rates) near the outlet of the chip and moved upstream with increasing flow rate. Therefore, we infer that the vortex shedding is amplified in the downstream direction, and the observed oscillations are a superposition of the wakes generated by individual pin fins. Once the amplitude of the oscillation exceeds a critical value, the recirculation zone between two successive pins starts to collapse and reform periodically (c.f. Fig. 7b). No transition was observed at the chip inlet location. Moreover, for the chip with a 1:1 height-to-pin diameter ratio, no vortex shedding was observed for Re_d up to 330 indicating a strong confinement effect of cavity walls. This confinement, however, resulted in a pressure drop that was higher than for $h/d = 2$. The pressure drop is a penalty resulting from the chip cooling process. Enhanced vortex shedding for lower pressure drop microcavities $h/d = 2$ compared to cavities with $h/d = 1$ also implies their potentially superior performance in heat transfer due to enhanced mixing. The flip side of this result for cavities with $h/d = 2$ is a larger resulting chip stack dimension. Clearly, a trade-off is required between chip dimension and enhanced vortex shedding, which could potentially enhance heat transfer due to mixing. A detailed investigation into heat transfer performance is currently underway in our laboratory.

Acknowledgments This work was partially supported by the Swiss Confederation through the SNSF evaluated RTD project nr. 618_67—CMOSAIC—funded by Nano-Tera.ch. The support is gratefully acknowledged. AR and MKT also acknowledge the fruitful discussions with Mr. Ashish Asthana and Dr. Igor Zinovik of LTNT, ETH Zurich.

References

Alfieri F, Tiwari MK, Zinovik I, Poulikakos D, Brunschwiler T, Michel B (2010) 3D integrated water cooling of a composite multilayer stack of chips. J Heat Trans 132(12):121402

Angele KP, Suzuki Y, Miwa J, Kasagi N (2006) Development of a high-speed scanning micro PIV system using a rotating disc. Meas Sci Technol 17:1639

Armellini A, Casarsa L, Giannattasio P (2009) Separated flow structures around a cylindrical obstacle in a narrow channel. Exp Therm Fluid Sci 33(4):604–619

Blonski S, Korczyk PM, Kowalewski TA (2007) Analysis of turbulence in a micro-channel emulsifier. Int J Therm Sci 46(11):1126–1141

Brunschwiler T et al (2009) Interlayer cooling potential in vertically integrated packages. Microsyst Technol 15(1):57–74

Iwaki C, Cheong K, Monji H, Matsui G (2004) PIV measurement of the vertical cross-flow structure over tube bundles. Exp Fluids 37(3):350–363

Koşar A, Mishra C, Peles Y (2005) Laminar flow across a bank of low aspect ratio micro pin fins. J Fluid Eng 127(3):419–430

Li H, Olsen MG (2006a) MicroPIV measurements of turbulent flow in square microchannels with hydraulic diameters from 200 μm to 640 μm. Int J Heat Fluid Fl 27(1):123–134

Li H, Olsen MG (2006b) Examination of large-scale structures in turbulent microchannel flow. Exp Fluids 40(5):733–743

Liang C, Papadakis G, Luo X (2009) Effect of tube spacing on the vortex shedding characteristics of laminar flow past an inline tube array: a numerical study. Comput Fluids 38(4):950–964

Lindken R, Rossi M, Grosse S, Westerweel J (2009) Micro-particle image velocimetry (μPIV): recent developments, applications, and guidelines. Lab Chip 9(17):2551

Meinhart CD, Zhang H (2000) The flow structure inside a microfabricated inkjet printhead. J Microelectromech S 9(1):67–75

Natrajan VK, Christensen KT (2007) Microscopic particle image velocimetry measurements of transition to turbulence in microscale capillaries. Exp Fluids 43(1):1–16

Natrajan VK, Christensen KT (2010) The impact of surface roughness on flow through a rectangular microchannel from the laminar to turbulent regimes. Microfluid Nanofluid 9:95–121

Nishimura T, Itoh H, Miyashita H (1993) The influence of tube layout on flow and mass transfer characteristics in tube banks in the transitional flow regime. Int J Heat Mass Tran 36(3):553–563

Olsen MG, Adrian RJ (2000) Out-of-focus effects on particle image visibility and correlation in microscopic particle image velocimetry. Exp Fluids 29:166–174

Özdemir MR, Koz M, Koşar A (2009) Parametric study on the effect of endwalls on fluid flow in micro pin-fins. 5th WSEAS ICACM, pp 54–59

Patil PP, Tiwari S (2010) Three-dimensional numerical investigations on flow and heat transfer for flow past a channel confined square cylinder. Prog Comput Fluid Dyn Int J 10(3):146–156

Paul SS, Tachie MF, Ormiston SJ (2007) Experimental study of turbulent cross-flow in a staggered tube bundle using particle image velocimetry. Int J Heat Fluid Fl 28(3):441–453

Perry JL, Kandlikar SG (2008) Fouling and its mitigation in silicon microchannels used for IC chip cooling. Microfluid Nanofluid 5(3):357–371

Prasher RS et al (2007) Nusselt number and friction factor of staggered arrays of low aspect ratio micropin-fins under cross flow for water as fluid. J Heat Trans 129:141–153

Raffel M, Willert C, Wereley C, Kompenhans J (2007) Particle image velocimetry: a practical guide, 2nd edn. Springer, Heidelberg

Santiago JG, Wereley ST, Meinhart CD, Beebe DJ, Adrian RJ (1998) A particle image velocimetry system for microfluidics. Exp Fluids 25(4):316–319

Sheen HJ, Hsu CJ, Wu TH, Chang CC, Chu HC, Yang CY, Lei U (2008) Unsteady flow behaviors in an obstacle-type valveless micropump by micro-PIV. Microfluid Nanofluid 4(4):331–342

Ulrich R, Brown WD (2006) Advanced electronic packaging, 2nd edn. IEEE Press, Piscataway

Wereley ST, Meinhart CD (2010) Recent advances in micro-particle image velocimetry. Annu Rev Fluid Mech 42:557–576

Ziada S, Oengören A (1993) Vortex shedding in an in-line tube bundle with large tube spacings. J Fluid Struct 7:661–687